

# A Theoretical/Experimental Study of Silicon Epitaxy in Horizontal Single-Wafer Chemical Vapor Deposition Reactors

Srikanth Kommu,<sup>a,b,\*</sup> Gregory M. Wilson,<sup>b,\*</sup> and Bamin Khomami<sup>a,z</sup>

<sup>a</sup>Department of Chemical Engineering and the Materials Research Laboratory, Washington University, St. Louis, Missouri 63130, USA

<sup>b</sup>MEMC Electronic Materials, Incorporated, Epitaxial Silicon Technology, St. Peters, Missouri 63376, USA

The main goal of this study is to examine the possibility of using detailed three-dimensional simulations of transport of momentum, energy, and mass in horizontal single-wafer epitaxial silicon reactors in conjunction with relatively simple kinetic models to describe the reactor's performance over the entire range of operating conditions. As the  $\text{SiHCl}_3\text{-H}_2$  system is a widely used precursor for epitaxial silicon deposition in industrial applications, we have chosen to focus our model development on this system. In the development of the model we have considered the dependence of the gas properties on the gas composition as well as on the temperature. In addition, mass transport due to thermal diffusion has been considered. The accuracy of the simulation model has been examined by comparing the predicted silicon deposition rates and profiles in two commercial chemical vapor deposition (CVD) reactors with the experimentally measured values. A comparison of simulation and experimental results has indicated that a detailed transport model in conjunction with a Langmuir-Hinshelwood type kinetic model for silicon deposition accurately describes the epitaxial silicon deposition rate and deposition profile. In turn, this lumped reaction kinetic model has been used for optimization of commercially available horizontal CVD reactors for epitaxial deposition of silicon.

© 2000 The Electrochemical Society. S0013-4651(99)06-070-X. All rights reserved.

Manuscript submitted June 14, 1999; revised manuscript received November 15, 1999.

Chemical vapor deposition (CVD) is a process that uses chemically reactive gases to deposit thin solid films on a surface. The use of these thin solid films is widespread in many industries such as microelectronics, magnetic materials, optical devices, automobiles, and ceramics. In the silicon-based semiconductor industry CVD is used to deposit a wide variety of films including polycrystalline silicon (polysilicon), epitaxial silicon, silicon oxides, and silicon nitrides. The advantage of the CVD process compared to other deposition processes such as evaporation, sputtering, etc., is that it is capable of producing thin films of a wide variety of materials with precisely defined and highly reproducible electrical, optical, chemical, and mechanical properties.<sup>1</sup>

The CVD process is a complex dynamical process involving simultaneous mass, momentum, and energy transport, and complex chemical reactions. Hence, the quality of the films produced will be determined by the interactions of various transport processes and the chemical reactions in the CVD chamber, which in turn depend on process conditions such as flow rates, pressure, temperature, concentration of chemical species, reactor geometry, etc. The modern microelectronics industry also put severe demands on the quality of films produced by the CVD process. The CVD film deposition techniques in the microelectronics industry need to fulfill general requirements such as high deposition rate, good thickness uniformity across a wafer (less than 2% thickness nonuniformity), minimum particulate generation, and economic use of reactants. In addition, the design and optimization of CVD reactors must fulfill the increasing demands in the semiconductor industry. However, due to the lack of detailed fundamental models the industrial CVD practitioners are frequently forced to rely on methods of trial and error as well as on statistical methods to create purely empirical models of the reactor behavior. The empirical relations that are produced following these procedures are difficult to use if the reactants or the reactor geometry is changed. On the other hand, mathematical modeling and simulation provide an excellent economic alternative to trial and error based experimental techniques. The immediate benefits to be realized are fewer experiments, reduction in waste during experimentation, and the ability to deal with different reactive species and reactor geometries. In addition, simulation models can be used for optimization of the process conditions and reactor geometry as well as for design of new processes for high volume production. The main

purpose of this study is to develop a detailed simulation model of silicon epitaxy in atmospheric horizontal single-wafer CVD reactors.

## Background

The CVD process is schematically shown in Fig. 1. In general, the highly interconnected processes that take place in a CVD reactor can be summarized as follows<sup>2</sup>: convective and diffusive transport of reactants from the reactor inlet to the wafer surface; chemical reactions in the gas-phase leading to new reactive species and by-products; convective and diffusive transport of the reactants and reaction products from the gas-phase reactions to the wafer surface; adsorption of gas-phase species on the wafer surface; surface diffusion of adsorbed species; heterogeneous surface reactions leading to the formation of a solid film; desorption of gaseous reaction products from the wafer surface; convective and diffusive transport of reaction products to the outlet of the reactor.

Different types of reactor chambers are used with different ranges of operating conditions for the purpose of CVD, *e.g.*, horizontal reactors, vertical reactors, pancake reactors, barrel reactors, continuous belt reactors, etc. However in recent years, the demand for silicon wafers that have a large diameter and meet the stringent specifications of the microelectronics industry is on the rise. This has led to increased interest in single-wafer reactors that are capable of producing high quality wafers, one wafer at a time. Hence, in this study we have focused our modeling efforts on horizontal single-

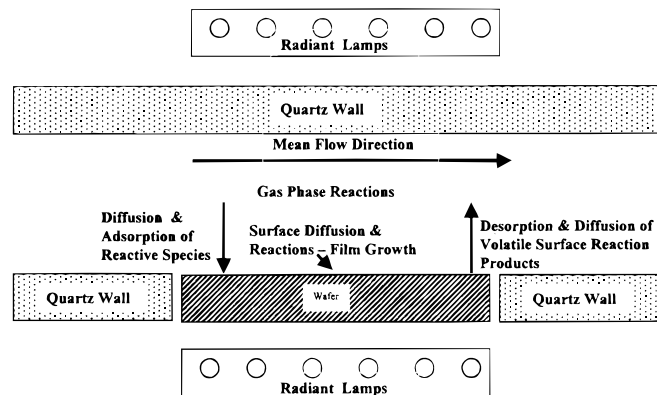


Figure 1. Schematic representation of a typical horizontal CVD reactor.

\* Electrochemical Society Active Member.

<sup>z</sup> E-mail: bam@poly1.che.wustl.edu

wafer epitaxial reactors. In what follows we briefly summarize the most relevant prior work performed in this area to put into context our own efforts.

One-dimensional as well as two-dimensional analyses of transport of mass, momentum, and energy have been used to examine the dynamics of various CVD reactors with different reaction kinetics.<sup>3-5</sup> Although these analyses have provided significant insight on how various parameters influence the dynamics of the deposition process, they are inadequate in describing the dynamics of horizontal single-wafer CVD reactors. This is mainly due to the presence of buoyancy driven recirculations that are created as a result of temperature gradients present in single-wafer reactors as well as due to a number of other factors such as edge and entrance effects.<sup>6,7</sup> Therefore, a number of previous investigators have focused their attention on development of three-dimensional simulation models of horizontal epitaxial CVD reactors. The first of such studies were performed by Mofat and Jenson<sup>8,9</sup> where the epitaxial deposition of silicon in a CVD reactor was simulated by using a reduced set of chemical reactions for silane decomposition. In general, their studies have demonstrated that three-dimensional transport effects play an important role in determining the silicon deposition profiles even in the absence of buoyancy driven cells due to the influence of different wall boundary conditions. Kleijn and Hoogendoorn<sup>10</sup> have also developed three-dimensional simulation models of horizontal CVD reactor for predicting GaAs deposition profiles. They demonstrated the relative importance of convection, diffusion, and thermal diffusion and found that three-dimensional models can accurately predict the experimental results under widely varying conditions. However, their study was limited to deposition processes that are completely transport limited.

Some of the above studies as well as others have demonstrated that although complex multiple reaction chemistry plays an important role in epitaxial CVD, deposition rates and profiles can be predicted accurately by models based on transport of only one reactive species.<sup>5,8,10-13</sup> Habuka *et al.*<sup>14-16</sup> have used this strategy to model a horizontal epitaxial silicon reactor. Specifically, they used a detailed transport model to predict averaged silicon deposition rates for a SiHCl<sub>3</sub> and H<sub>2</sub> precursor and found that the nonlinear increase in the average silicon deposition rate is due to the increase in molecular weight of the inlet SiHCl<sub>3</sub> and H<sub>2</sub> gas mixture which can be predicted using a Eley-Rideal type decomposition model for SiHCl<sub>3</sub>. Habuka *et al.*<sup>16</sup> also compared their model predictions with experiments in terms of an average silicon deposition rate that takes into account the effect of wafer rotation. However, this is inappropriate since wafer rotation only leads to azimuthal averaging but not radial averaging of silicon deposition rates. A more appropriate comparison would involve measuring deposition rates as a function of inlet gas composition for a fixed inlet gas flow rate and as a function of inlet gas flow rate for a fixed gas composition. By following this strategy one can decouple the effect of gas flow rate and composition on silicon deposition rates and hence perform a detailed comparison of model predictions and experimental measurements.

The above summary has clearly shown that three-dimensional modeling for CVD reactors for transport-limited systems<sup>10</sup> as well as for systems such as silane whose chemistry is well understood<sup>8</sup> has been successfully used to describe the reactor dynamics. However, for systems such as the SiHCl<sub>3</sub>-H<sub>2</sub> mixture whose chemistry of decomposition is not well understood, the success of 3D modeling efforts in describing the dynamics of the reactor is uncertain.

Our aim in this study is to examine the predictive capability (*i.e.*, in terms of silicon deposition rate and deposition profiles) of detailed three-dimensional simulation models of horizontal single-wafer epitaxial silicon reactors with simple kinetic models for decomposition of SiHCl<sub>3</sub>. We have selected to study the SiHCl<sub>3</sub>-H<sub>2</sub> mixture not only because this system is widely used for growing epitaxial films in industrial applications but also because the decomposition chemistry of SiHCl<sub>3</sub> is not well understood. Hence, by performing simulations with various kinetic models and comparing the simulation results with experimental measurements a more complete picture of SiHCl<sub>3</sub> decomposition can be obtained. In the development of the model we

have considered the dependence of the gas properties on the gas composition as well as on the temperature. In addition, mass transport due to thermal diffusion has been considered. To examine the accuracy of the simulation model, we have performed experiments in two commercial CVD reactors. Specifically, deposition rates have been measured at atmospheric pressure and various wafer temperatures as a function of inlet gas composition for a fixed inlet volumetric flow rate as well as a function of inlet gas flow rate for a fixed inlet gas composition. A detailed comparison of simulation and experimental results has indicated that a detailed transport model in conjunction with a Langmuir-Hinshelwood type kinetic model for silicon deposition accurately describes the epitaxial silicon deposition process. In turn, this lumped reaction kinetic model has also been used for optimization of commercially available horizontal CVD reactors used for epitaxial deposition of silicon.

### Problem Formulation

In order to develop an accurate simulation model that fully describes the transport and deposition of chemical species in a CVD reactor one needs to solve the appropriate set of governing equations under realistic boundary conditions. These governing equations must accurately describe the gas flow, transport of energy and chemical species, and the chemical reactions in a CVD reactor. As shown by earlier studies<sup>1,10</sup> the dependence of gas properties on gas composition and temperature as well as transport due to thermal diffusion should be considered. Taking all of these factors into consideration, the governing equations have been arrived at by using the following realistic assumptions for atmospheric pressure CVD: the gases are considered to be ideal obeying the ideal gas law and Newton's law of viscosity; the gas mixture is assumed to behave as a continuum (Knudsen number < 0.01); the heat generated/consumed by chemical reactions is neglected as the reactants are highly diluted; heating due to viscous dissipation is neglected (Brinkman number < 0.01); pressure variations in the energy equation are neglected as the Mach numbers are very small; the Reynolds number and the Rayleigh number are not very large so the gas flow is assumed to be laminar; the Dufour effect which causes an energy flux in a gas mixture as a result of concentration gradients, is neglected.

*Governing equations.*—We are interested in determining the steady-state silicon deposition rate distribution on a wafer so we have derived the governing set of equations at steady state. However, as the governing set of equations and boundary conditions contain several parameters, it is advantageous to write them in dimensionless form. In order to make the governing set of equations dimensionless, the following dimensionless variables are introduced

$$\hat{U} = \frac{U}{V} \quad \hat{T} = \frac{T}{T_{\text{wafer}}} \quad \hat{w}_A = \frac{w_A}{w_{A,\text{in}}} \quad \hat{P} = \frac{P_{\text{Ref}}}{\rho V^2} \quad \hat{\nabla} = \nabla L$$

$$\hat{\rho} = \frac{\rho}{\rho_{\text{Ref}}} \quad \hat{\mu} = \frac{\mu}{\mu_{\text{Ref}}} \quad \hat{\lambda} = \frac{\lambda}{\lambda_{\text{Ref}}} \quad \hat{C}_p = \frac{C_p}{C_{p,\text{Ref}}}$$

$$\hat{D}_{AB} = \frac{D_{AB}}{D_{AB,\text{Ref}}} \quad \hat{D}_A^T = \frac{D_A^T}{D_{A,\text{Ref}}^T} \quad [1]$$

All the reference properties are calculated at a reference temperature  $T_{\text{Ref}}$ ,  $V$  is the characteristic velocity of the gas, and  $L$  is the characteristic reactor dimension. A summary of all the symbols used is given in the List of Symbols at the end of this paper. Using the above dimensionless parameters, the governing equations take the following dimensionless forms

Mass balance

$$\hat{\nabla} \cdot \hat{\rho} \hat{U} = 0 \quad [2]$$

Chemical species balance

$$\hat{\nabla} \cdot (\hat{\rho} \hat{U} \hat{w}_A) = \frac{1}{Re \cdot Sc} \hat{\nabla} \cdot (\hat{\rho} \hat{D}_{AB} \hat{\nabla} \hat{w}_A) + \frac{1}{Re \cdot Td} \hat{\nabla} \cdot \left( \frac{\hat{D}_T}{T} \hat{\nabla} \hat{T} \right) \quad [3]$$

Momentum balance

$$\hat{\nabla} \cdot (\hat{\rho} \hat{U} \hat{U}) = \frac{1}{Re} \hat{\nabla} \cdot \left( -\frac{2}{3} \hat{\mu} \left[ \hat{\nabla} \cdot \hat{U} \right] I + \hat{\mu} \left[ \hat{\nabla} \cdot \hat{U} + (\hat{\nabla} \cdot \hat{U})^T \right] \right) - \hat{\nabla} \hat{P} + \frac{Gr}{Re^2} \left( \frac{\hat{T} - \frac{1}{2}}{\left( \hat{T} - \frac{1}{2} \right) Ga + 1} \right) \hat{e}_z \quad [4]$$

Energy balance

$$\hat{C}_p \hat{\nabla} \cdot (\hat{\rho} \hat{U} \hat{T}) = \frac{1}{Re \cdot Pr} \hat{\nabla} \cdot (\hat{\rho} \hat{\nabla} \hat{T}) \quad [5]$$

where

$$Re = \frac{\rho_{Ref} VL}{\mu_{Ref}} \quad Gr = \frac{g \rho_{Ref} L^3 T_{wafer}}{\mu_{Ref}^2 T_{Ref}} \quad Pr = \frac{\mu_{Ref} C_{p,Ref}}{\lambda_{Ref}} \quad Ga = \frac{T_{wafer}}{T_{Ref}} \quad [6]$$

$$Sc = \frac{\mu_{Ref}}{\rho_{Ref} D_{Ref}} \quad Td = \frac{\mu_{Ref} W_{A,in}}{D_{Ref}^T} \quad [7]$$

In order to calculate the transport properties of the gas mixture in the above equations, the transport properties of the constituent species must be known. From the DIPPR database<sup>17</sup> we have obtained the data for specific heat, viscosity, and thermal conductivity of relevant gas species as a function of temperature. In turn, we have used polynomial functions to fit these data as functions of temperature (see Appendix A). The binary diffusion coefficients and the thermal diffusion coefficients were estimated using kinetic theory and the variation of these properties with temperature have also been determined (see Appendix B).

It can be seen from the above equations that the flow and the temperature fields in the reactor are determined by four dimensionless groups, viz.,  $Re$ ,  $Gr$ ,  $Pr$ , and  $Ga$  while the species transport is determined by  $Re$ ,  $Sc$ , and  $Td$ . The range of these dimensionless groups

in atmospheric pressure CVD is given in Table I. In this study we have considered the effect of all relevant dimensionless groups on the flow, temperature, and concentration profiles in the reactor, and by doing so we have fully characterized the reactor dynamics over the entire range of operating conditions. The results of these studies are presented in the section on Results and Discussion.

**Reactor geometry.**—Figure 2 is a schematic representation of the ASM Epsilon One single-wafer epitaxial silicon reactor and Fig. 3 is a schematic representation of the Applied Materials' Centura reactor. These reactors have been used in our experimental studies of epitaxial deposition of silicon on silicon wafers. The dimensions of the reactors are shown in the figures, and a description of the computational domain used to simulate the deposition process in these reactors is given in the Results and Discussion section. In what follows, a brief description of how silicon is epitaxially deposited on a wafer in these commercial reactors is given.

In both these reactors, the gases are injected at room temperature (25°C) through the three inlets (inlet 1, inlet 2, and inlet 3) in the gas injector. The gases then pass through the quartz reactor chamber, which contains a silicon wafer placed on a graphite susceptor and surrounded by a SiC ring. The wafer is heated radiatively by lamp arrays placed outside the quartz reactor chamber such that the wafer temperature is maintained a constant (1398 K is a typical wafer temperature). The gases react in the chamber depositing the desired solid silicon film on the surface of the wafer. Finally, the reactant and product gases leave the reactor through the outlet, which is fixed at atmospheric pressure. The exterior surfaces of the reactor are cooled with recirculated air.

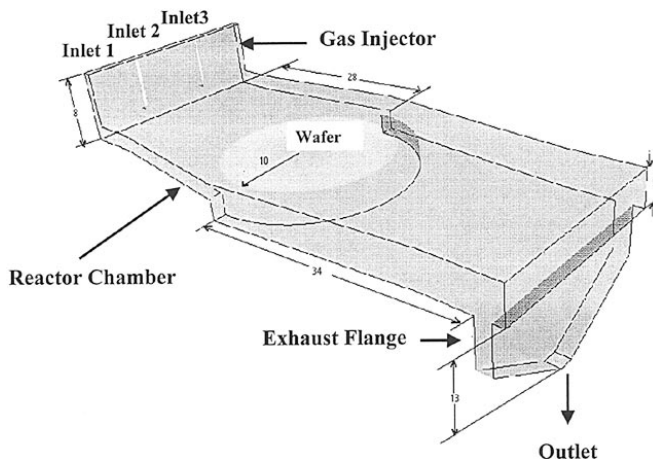


**Figure 2.** Schematic representation of ASM Epsilon One single-wafer epitaxial silicon reactor. All dimensions are in centimeters.

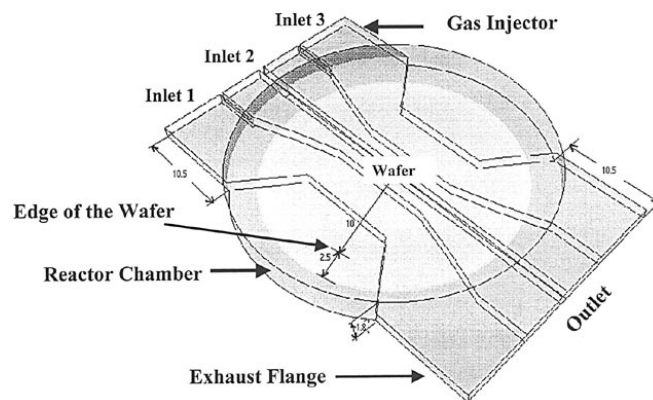


**Figure 3.** Schematic representation of Applied Materials' Centura single-wafer epitaxial silicon reactor. All dimensions are in centimeters.

**Table I. Important dimensionless groups and their range in atmospheric CVD reactors.**

Dimensionless group	Definition	Range
Reynolds number ( $Re$ )	Inertial forces/viscous forces	5-100
Schmidt number ( $Sc$ )	Momentum diffusivity/chemical species diffusivity	0.1-10
Thermal diffusion number ( $Td$ )	Momentum diffusivity/chemical species diffusivity due to temperature gradients	0.1-10
Heat transfer pecllet number ( $Pe_H$ )	Convective heat transfer/diffusive heat transfer	1.5-70
Mass transfer pecllet number ( $Pe_M$ )	Convective mass transfer/diffusive mass transfer	0.5-1,000
Surface arrhenius number ( $Ar$ )	Activation energy/potential energy	10-30
Grashof number ( $Gr$ )	Buoyancy forces/viscous forces	100-100,000
Prandtl number ( $Pr$ )	Momentum diffusivity/thermal diffusivity	0.3-0.7
Gay-Lussac number ( $Ga$ )	Temperature difference/reference temperature	1-1.3
Rayleigh number ( $Ra$ )	Buoyancy forces/viscous forces	30-70,000
Surface Damkohler number ( $Da$ )	Chemical reaction rate/diffusion rate	0.1-500

**Boundary conditions.—Walls.**—No slip boundary condition for the gas velocity is specified

$$\hat{\mathbf{U}} = 0 \quad [8]$$

Different thermal boundary conditions have been used on the walls of the reactor, *i.e.*

$$\hat{T} = \hat{T}_{\text{wall}} \quad \text{or} \quad \mathbf{n} \cdot \hat{\nabla} \hat{T} = 0 \quad \text{or} \quad \mathbf{n} \cdot \hat{\nabla} \hat{T} = \hat{h}(\hat{T} - \hat{T}_{\text{inf}}) \quad [9]$$

Zero total mass flux for each of the chemical species is specified

$$\mathbf{n} \cdot (\mathbf{j}_A^{\hat{C}} + \mathbf{j}_A^{\hat{T}}) = 0 \quad [10]$$

**Wafer.**—No slip boundary condition for the gas velocity is specified or a wafer rotating speed is specified

$$\hat{\mathbf{U}} = 0 \quad \text{or} \quad \hat{\mathbf{U}}_{\text{wafer}} \quad [11]$$

An isothermal boundary condition is employed since the temperature of the wafer is maintained constant through radiative heating by the lamps

$$\hat{T} = \hat{T}_{\text{wafer}} \quad [12]$$

Based on the stoichiometry and an overall surface reaction leading to silicon deposition [*i.e.*,  $\text{SiHCl}_3(\text{g}) + \text{H}_2(\text{g}) \rightarrow \text{Si}(\text{s}) + 3\text{HCl}(\text{g})$ ], the mass consumption and generation of each chemical species is taken into account

$$\mathbf{n} \cdot (\mathbf{j}_A^{\hat{C}} + \mathbf{j}_A^{\hat{T}}) = \hat{R}_A \quad [13]$$

**Inlets.**—At the inlets the inlet velocity, temperature, and the composition of the gas mixture are specified, *i.e.*

$$\hat{\mathbf{U}} = \hat{\mathbf{U}}_{\text{in}} \quad [14]$$

$$\hat{T} = \hat{T}_{\text{in}} \quad [15]$$

$$\hat{C}_A = \hat{C}_{A,\text{in}} \quad [16]$$

**Outlets.**—At the outlets the flow is assumed to be fully developed

$$\mathbf{n} \cdot \hat{\nabla} \cdot \hat{\mathbf{U}} = 0 \quad [17]$$

$$\mathbf{n} \cdot \hat{\nabla} \hat{T} = 0 \quad [18]$$

$$\mathbf{n} \cdot \hat{\nabla} \hat{C}_A = 0 \quad [19]$$

### Computational Details

Due to the very large temperature gradients present near the silicon wafer in the reactor, the body force term in the momentum balance equation has not been approximated using the Boussinesq method. Instead the density in the buoyancy term is written as

$$\rho = \rho_0 + (\rho - \rho_0) \quad [20]$$

where  $\rho_0$  is a reference density calculated at the reference gas temperature, and the term  $\rho_0 g$  is absorbed into the pressure gradient term of Eq. 4. In turn, the set of governing equations have been discretized using the finite volume technique and the SIMPLEC algorithm has been used for pressure corrections.<sup>17,18</sup> Specifically, an in-house developed Fortran code (*i.e.*, for specific reaction kinetics) coupled with a commercially available software package CFX 4.1c from AEA Technology, Inc.,<sup>17</sup> has been used to perform the computations. It should be noted that the discretization of the governing equations results in a set of coupled nonlinear algebraic equations. In order to reduce the required computational resources, a two-level iteration technique has been employed to solve these nonlinear equations. Specifically, an inner iteration loop is used to solve for the spatial coupling of each variable, and an outer loop is used to solve for the coupling between variables. The convergence criteria for this iterative procedure requires the error in the continuity equation to fall below 0.1% of the total mass flow rate entering the system. In addition, the residuals of all other variables such as velocity, pressure, and enthalpy are required to be less than  $10^{-8}$ .

Two different solvers have been used throughout this study. One solver is based on the Stone's method<sup>19</sup> and the other is based on the algebraic multigrid method.<sup>20</sup> The solver using Stone's method generally proved to be faster than the solver based on the algebraic multigrid method, however, the multigrid solver which solves the discretized equations on a series of coarsening meshes proved to be more robust for cases where the buoyancy term in the momentum equation is dominant.

### Experimental

To determine the variation in the silicon deposition rate as a function of different operating conditions (*i.e.*, temperature of the wafer, initial concentration of  $\text{SiHCl}_3$ , gas flow rates, and the ratio of gas flow rates across the three inlets of the reactors and rotation rate of the wafer) a series of experiments in the commercial CVD reactors shown schematically in Fig. 2 and 3 were conducted. The following procedure has been used in performing all the epitaxial silicon deposition experiments. In both reactors, first hydrogen gas was injected into the reactor through the three inlets (inlet 1, inlet 2, and inlet 3) in the gas injector at a constant flow rate (60 slm is a typical value of the gas flow rate). Then the radiative lamps located outside the reactor were switched on so that the silicon-coated graphite susceptor, surrounded by the SiC ring was heated to about 700°C. Then the silicon wafer is loaded into the reactor and placed on top of the susceptor, and the power of the lamps is increased to obtain a wafer temperature of 1125°C. Once this protocol was completed, the flow of hydrogen gas into the reactor was replaced by a gas mixture of  $\text{SiHCl}_3$  and  $\text{H}_2$  (a typical value of flow rate is 80 slm of  $\text{H}_2$  and 20 g/min of  $\text{SiHCl}_3$ ). The gases then pass through the quartz reactor chamber, which contains the silicon wafer with a constant surface temperature of 1125°C. The gases react in the chamber depositing the solid silicon epitaxial film on the surface of the wafer. Clearly, the deposited layer thickness depends on the deposition time. In all the experiments, the deposition time was fixed at 100 s for all different combinations of  $\text{H}_2$  and  $\text{SiHCl}_3$  flows. This leads to a steady-state epitaxial silicon deposition rates of about 4  $\mu\text{m}/\text{min}$ . After the deposition step, the flow of  $\text{SiHCl}_3$  is switched off so that only hydrogen gas flows through the reactor and the temperature of the wafer is ramped down to about 700°C. Then the wafer is unloaded and the epitaxial silicon thickness is measured using Fourier transform infrared (FTIR) spectroscopy.<sup>21</sup> It should be noted that after each deposition step, the whole quartz chamber is etched with HCl to remove any chamber deposits on the reactor walls. In all the above experiments, reactant and product gases leave the reactor chamber through the outlet, which is fixed at atmospheric pressure and the exterior surfaces of the reactor are continuously cooled with recirculated air. The results of these experiments are reported in next section.

### Results and Discussion

**Influence of operating conditions on the reactor performance.**— In this section, we discuss the effect of operating conditions on the dynamics of atmospheric CVD reactors. The purpose of this investigation is to determine the operating conditions that will result in deposition of a uniform silicon layer.

In general the gases used in atmospheric CVD applications have very similar Prandtl numbers, thus variations in the Prandtl number does not play an important role in the proper description of the process conditions (see Table I). Similarly the Gay-Lussac number only varies by a small amount. Therefore, the flow in the reactor is basically governed by the Reynolds and the Grashof numbers while the chemical species transport is dictated by Reynolds, Grashoff, Schmidt, and thermal diffusion numbers. As is the case in most industrial practices, the composition of  $\text{SiHCl}_3$ - $\text{H}_2$  gas mixture is chosen such that  $\text{SiHCl}_3$  is dilute in  $\text{H}_2$ . Hence it is possible to just solve for the flow and temperature fields initially and then use the computed flow and temperature fields to solve the chemical species balance equations. However, the advantage of using this decoupled technique in terms of overall central processing unit (CPU) time is very minor, hence we have solved all the governing equations simultaneously.

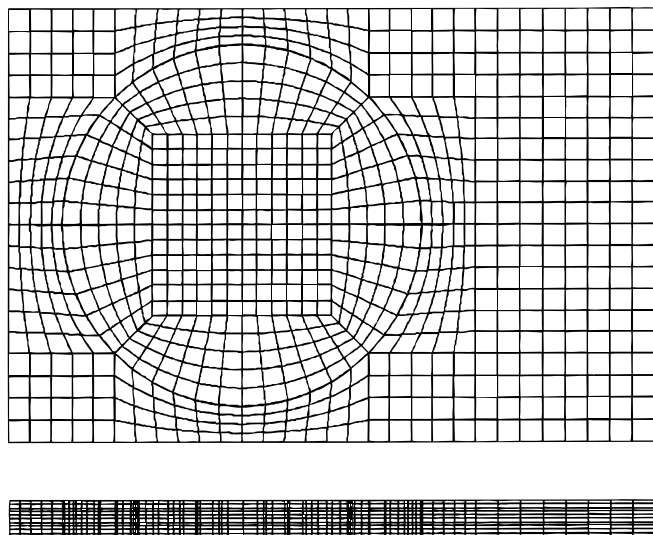


**Figure 4.** Domain discretization for the rectangular reactor geometry. The total number of finite volume cells equals 8,400. Top: projection of the mesh along the X-Y midplane; bottom: projection of the mesh along the X-Z midplane.

Figure 4 shows a typical mesh used in simulating the dynamics of a simple rectangular reactor. This simple reactor geometry has been selected to demonstrate the effect of different dimensionless groups on the performance of the reactor. The total number of finite volumes in the domain is equal to 8,400 and typical CPU times for numerical convergence of the coupled overall mass, momentum, and energy equations is on the order of 100 s on a Silicon Graphics Indigo2 workstation. Using this solution as an initial guess, and coupling the chemical species balance equations with the conservation equations for mass, momentum, and energy leads to a converged numerical solution in approximately 100 s. To ensure that the solutions generated with the mesh shown in Fig. 4 are accurate, selected computations using a much more refined mesh consisting of 200,000 cells were performed. Overall, we did not find a significant difference between the results from the two meshes, *i.e.*, the maximum difference between the computed results is less than 2%. Hence, the results shown below are based on the mesh shown in Fig. 4.

The effect of various dimensionless groups on the reactor performance has been studied by varying the reactor dimensions, wall boundary conditions, total pressure, as well as the carrier gas, and its flow rate. As mentioned earlier, the most important parameters that govern the reactor performance are  $Re$ ,  $Gr$ ,  $Sc$ , and  $Td$ . In Fig. 5 and 6, the effect of varying  $Re$  is illustrated. Specifically, Fig. 5a and b show the velocity vectors parallel and perpendicular to the mean flow direction under conditions of  $Re = 1$  and  $Gr = 1000$ . As expected, for a large Grashof number and a small Reynolds number recirculation cells in planes parallel and perpendicular to the mean flow direction are observed. Figure 5c depicts the temperature contours along the X-Z midplane plane. As clearly shown by this figure, the temperature field is uniform above the wafer surface which is a consequence of the fact that the heat transfer due to conduction is dominant compared to convection ( $Pe_H = 0.7$ ). Figure 5c also shows that near the edges of the wafer (where the recirculation cell is present) the temperature contours have slightly expanded leading to sections of uniform temperature in the recirculatory regions. Figures 6a and b demonstrate that as  $Re$  is increased (*i.e.*, from  $Re = 1$  to  $Re = 30$ ), but  $Gr$  is held constant (*i.e.*,  $Gr = 1000$ ) the recirculation cells disappear, *i.e.*, the flow profile is not greatly disturbed by the sudden heating at the leading edge of the wafer. However, it should be noted that the slight rearrangement observed in the velocity vectors is a direct consequence of the change in viscosity as a result of change in the temperature profile. These figures clearly show that changes in the ratio of  $Gr/Re^\beta$  (where  $1 \leq \beta \leq 2$ ) strongly influ-

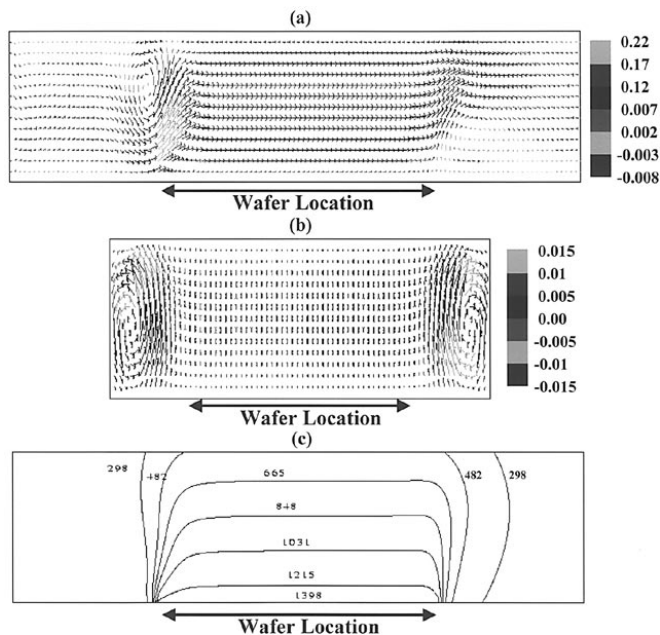


**Figure 5.** Velocity vector and temperature contour plots in the rectangular reactor geometry ( $Re = 1$ ,  $Gr = 1000$ ). (a) Velocity vector,  $U_x$  along the X-Z midplane; (b) velocity vector,  $U_y$  along the Y-Z midplane; (c) temperature contour along the X-Z midplane. The dimension along the Z axis has been magnified five times. Lines with no arrows correspond to velocities perpendicular to the plane in which plots have been made.

ence the formation of buoyancy induced recirculations. In fact simulations under conditions where inertial effects are important indicate the buoyancy driven recirculations can be avoided in this rectangular reactor geometry if the  $Gr/Re^2$  is maintained below 10. However, for some conditions which are uncommon for epitaxial CVD, *i.e.*, relatively high  $Ra$  ( $Ra > 1700-2800$ )<sup>5,10</sup> the flow becomes

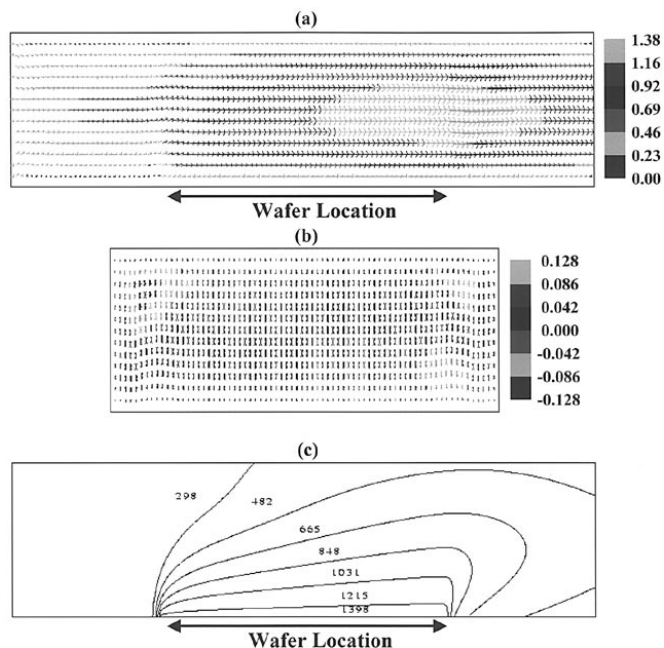


**Figure 6.** Velocity vector and temperature contour plots in the rectangular reactor geometry ( $Re = 30$ ,  $Gr = 1000$ ). (a) velocity vector,  $U_x$  along the X-Z midplane; (b) velocity vector,  $U_y$  along the Y-Z midplane; (c) temperature contour along the X-Z midplane. The dimension along the Z axis has been magnified five times. Lines with no arrows correspond to velocities perpendicular to the plane in which plots have been made.

unstable, and for these conditions the ratio of  $Gr/Re^2$  is not an appropriate indicator of the flow kinematics inside the reactor.

As mentioned earlier, heat transfer due to radiation is not considered in this study although it can be incorporated. However, we have chosen not to include radiation effects in the simulations because it would lead to a tremendous increase in the CPU time required for the computations. Hence, an attempt has been made to determine an appropriate wall boundary condition for heat transfer that can quantitatively describe the temperature distribution on the reactor chamber surfaces. Specifically, by performing simulations with different temperature boundary conditions, we have determined that a Robin-type of boundary condition (see the third boundary condition in Eq. 9) with a heat transfer coefficient of  $50 \text{ W m}^{-2} \text{ K}^{-1}$ , is adequate in predicting the measured temperatures at the reactor walls. Hence, this boundary condition has been used on the reactor walls for all the simulations described below.

As the performance of the reactor is determined by  $Re$ ,  $Gr$ ,  $Pr$ ,  $Ga$ ,  $Sc$ , and  $Td$ , we have systematically varied them to determine their effect on silicon deposition rate on the wafer using a simple reaction mechanism



The rate of the above reaction is assumed to be first-order in  $\text{SiHCl}_3$  concentration. It should be noted that although the above kinetic model does not fully describe the complex surface reactions that take place in the deposition process it can be used to qualitatively investigate the effect of different parameters on silicon deposition rate and thickness uniformity across a wafer. In all simulations discussed below, the Damkohler number defined based on the inlet  $\text{SiHCl}_3$  concentration, height of the reactor, and the rate of surface reaction was fixed at 100, *i.e.*

$$Da^s = \frac{LR_{\text{Si}}}{C_{\text{SiHCl}_3, \text{in}} D_{\text{SiHCl}_3-\text{H}_2}} = 100 \quad [22]$$

The reason for selecting this Damkohler number is that at higher Damkohler numbers the rate of mass flux of  $\text{SiHCl}_3$  to the wafer surface is the controlling factor for determining the silicon deposition rate compared to the intrinsic kinetics of  $\text{SiHCl}_3$  decomposition. Moreover, when the Damkohler number is small (*i.e.*,  $Da^s \ll 1$ ) the gas flow will have little or no effect on silicon thickness profile on the wafer. Under these conditions, the silicon deposition rate will be dictated by the wafer surface temperature uniformity since the deposition process is controlled by reaction kinetics.

Figure 7 shows the effect of  $Re$  on silicon deposition rate in the flow direction along the centerline of the wafer for a fixed  $Gr = 1000$  and a fixed  $Sc = 1.2$ . As shown by this figure the silicon depo-

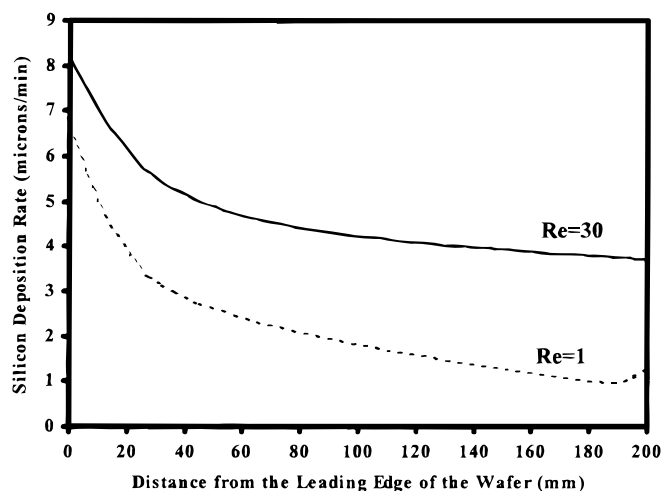


Figure 7. Silicon deposition rate in the flow direction along the centerline of the wafer as a function of  $Re$  ( $Gr = 1000$ ,  $Sc = 1.2$ ).

sition rate increases with an increase in  $Re$  (*i.e.*,  $Pe_M$  is increased). This is due to the increase in the rate of mass flux of  $\text{SiHCl}_3$  to the wafer surface. Moreover, an increase in  $Re$  has a pronounced effect on the deposition rate profile, *i.e.*, with an increase in  $Re$  the variations in the deposition rate from the leading edge to the trailing edge of the wafer decrease. These results can be rationalized in the following manner. For  $Pe_M = 1.2$ , the residence time of the gas in the reactor is greater in comparison to higher values of  $Pe_M$  as a result more of  $\text{SiHCl}_3$  is converted near the leading edge of the wafer hence,  $\text{SiHCl}_3$  is severely depleted down the length of the wafer. The increase in the deposition rate at the trailing edge of the wafer for  $Pe_M = 1.2$  is due to the presence of the buoyancy driven recirculation cell in that location (see Fig. 5a).

In Fig. 8 the effect of variations of thermal diffusion ( $Td$ ) on silicon deposition rate for a fixed  $Re = 30$ ,  $Sc = 1.2$ , and  $Gr = 1000$  is shown. Figure 8 clearly shows that when  $Td$  is small the silicon deposition rate is unaffected by thermal diffusion, however, a significant increase in  $Td$  leads to lower deposition rates. To clearly demonstrate the effect of thermal diffusion one needs to examine the mass fraction profiles of  $\text{SiHCl}_3$  inside the reactor under different conditions. Figure 9 shows the mass fraction profile of  $\text{SiHCl}_3$  along the  $X$ - $Z$  mid-plane passing through the center of the wafer in the reactor (for an initial  $\text{SiHCl}_3$  mass fraction = 0.72). As shown by this figure, although the initial mass fraction of  $\text{SiHCl}_3$  is 0.72, due to thermal diffusion the  $\text{SiHCl}_3$  concentration near the surface of the wafer decreases. This effect can be more clearly demonstrated by considering thermal diffusion in the absence of surface reaction. Figure 10 shows the simulation results in the absence of surface reaction. Figure 10 clearly demonstrates that the  $\text{SiHCl}_3$  concentration becomes smaller near the surface of the wafer although no consumption of  $\text{SiHCl}_3$  at the hot wafer surface is taking place. This is due to the fact that  $\text{SiHCl}_3$  molecules are much heavier than  $\text{H}_2$  molecules and the temperature gradient between wafer and the surroundings will lead to the transport of

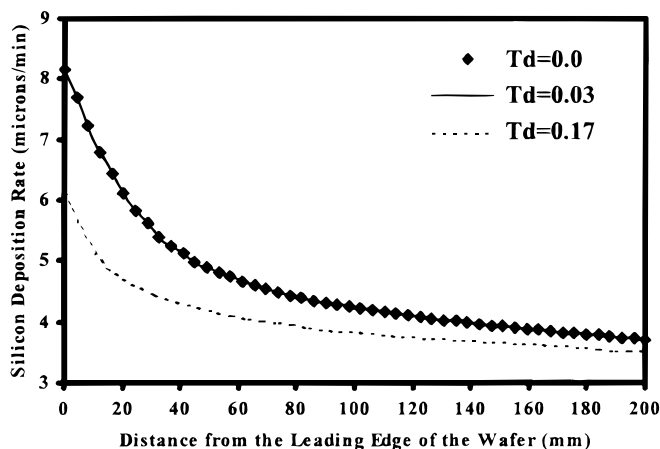


Figure 8. Effect of thermal diffusion on silicon deposition rates in the flow direction along the centerline of the wafer ( $Re = 30$ ,  $Gr = 1000$ ,  $Sc = 1.2$ ). The dimension along the  $Z$  axis has been magnified five times.

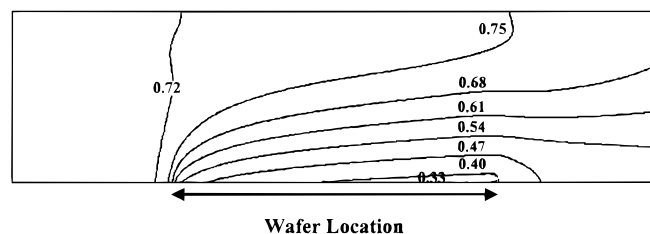
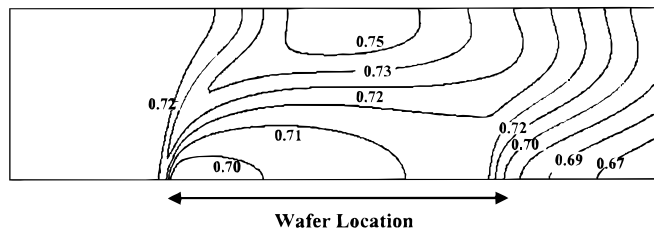


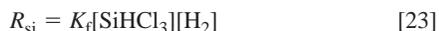
Figure 9. Mass fraction profile of  $\text{SiHCl}_3$  along the  $X$ - $Z$  midplane in the rectangular reactor geometry in the presence of surface reaction ( $w_{\text{SiHCl}_3, \text{in}} = 0.72$ ). The dimension along the  $z$  axis has been magnified five times.



**Figure 10.** Mass fraction profile of  $\text{SiHCl}_3$  along the  $X$ - $Z$  midplane in the rectangular reactor in the absence of surface reaction ( $w_{\text{SiHCl}_3, \text{in}} = 0.72$ ). The dimension along the  $Z$  axis has been magnified five times.

$\text{SiHCl}_3$  molecules away from the hot wafer surface. Figure 10 also shows that the concentration becomes even smaller beyond the trailing edge of the wafer, which is due to the huge temperature gradients in this region. Overall, these simulations clearly demonstrate that thermal diffusion must be included in the simulation model if accurate predictions of transport of the chemical species and the deposition rates are desired over the entire range of operating conditions.

*Silicon deposition rate measurements and predictions.*—An accurate kinetic model for  $\text{SiHCl}_3$  decomposition needs to be coupled with the above described transport model to predict silicon deposition rates as a function of different operating parameters. There is a reasonable amount of information available regarding intrinsic kinetic and thermochemical information on chlorosilanes in the physical chemistry literature. Ho *et al.*<sup>22</sup> have recently performed a comprehensive review of prior studies<sup>23-28</sup> dealing with gas-phase and surface chemistry of  $\text{SiHCl}_3$ , and proposed a reaction mechanism for the  $\text{SiHCl}_3$  kinetics. The key observations made by Ho *et al.*<sup>22</sup> are as follows: the mass flux of  $\text{SiHCl}_3$  is greatly responsible for the silicon deposition rate; the deposition rate is insensitive to the rate of  $\text{H}_2$  and  $\text{HCl}$  adsorption/desorption; the concentration of gas-phase intermediates such as  $\text{SiCl}_2$  is very small. Although it is possible to couple the reaction mechanism proposed by Ho *et al.*<sup>22</sup> with a detailed three-dimensional transport model, it is not practical to perform reactor design and optimization with such a model since many simulations have to be performed to deal with the uncertainties present in the surface reaction rates. As an alternative we have decided to use a lumped reaction kinetic model that can capture the important observations made by Ho *et al.*<sup>22</sup> First, an attempt was made to use the simplest possible kinetic model which consists of an overall surface reaction given by Eq. 21 where the rate of reaction is assumed to be first order in  $\text{SiHCl}_3$  and  $\text{H}_2$  concentrations, *i.e.*

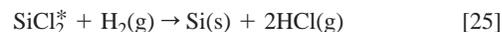


However, using the above reaction kinetics in the simulations did not lead to a good comparison between model predictions and experimental results (the results are shown in Fig. 13, 14, and 15). It should be noted that  $K_{\text{f}}$  in Eq. 23 is determined using a regression analysis which is described in more detail later in this section. Clearly, the simple kinetic model shown in Eq. 23 is incapable of taking into account one of the key observations made by Ho *et al.*<sup>22</sup> namely, the deposition rate is sensitive to the desorption rate of  $\text{H}_2$ . To take this into account, we have used a Langmuir-Hinshelwood kinetic model to describe the surface chemistry and in what follows, the approach used to simplify the reaction chemistry of  $\text{SiHCl}_3$  decomposition to the Langmuir-Hinshelwood kinetic model is described. The silicon surface is assumed to have a fixed number of reactive sites. The reactants, *i.e.*,  $\text{SiHCl}_3$  molecules, are transported from the gas phase to the surface of the silicon wafer.  $\text{SiHCl}_3$  molecules then attack the unoccupied reactive sites and decompose at a certain rate according to the following reaction



Equation 24 describes the adsorption reaction mechanism where  $\text{SiCl}_2^*$  is the adsorbed species (we assume that the adsorption is limited to only one monolayer, and there is no interaction between the

adsorbed molecules). The adsorbed  $\text{SiCl}_2^*$  species is most likely bonded to the wafer surface with the two chlorine atoms pointing to the gas stream. Therefore, after adsorption one ends up with a silicon surface covered with chlorine atoms. This adsorbed layer is then attacked by the hydrogen atoms to reduce  $\text{SiCl}_2^*$  to  $\text{Si}$  and release  $\text{HCl}$  gas according to the following reaction



The rate of adsorption of  $\text{SiHCl}_3$ ,  $R_{\text{ad}}$ , on the silicon wafer surface (see Eq. 24) is assumed to be first-order in  $\text{SiHCl}_3$  concentration and is given by

$$R_{\text{ad}} = K_{\text{ad}}(1-X)C_{\text{SiHCl}_3}^{\text{s}} \quad [26]$$

In Eq. 26,  $X$  denotes the fraction of the sites occupied by  $\text{SiHCl}_3$ ,  $C_{\text{SiHCl}_3}^{\text{s}}$  denotes the  $\text{SiHCl}_3$  concentration at the surface of the silicon wafer, and  $K_{\text{ad}}$  denotes the adsorption rate constant, which is a function of temperature. The rate of decomposition of the adsorbed  $\text{SiCl}_2^*$ , which is the same as the rate of formation of silicon from  $\text{SiCl}_2^*$ , is assumed to be first order in  $\text{H}_2$  concentration at the surface of the silicon wafer and is given by

$$R_{\text{Si}} = K_{\text{r}}XC_{\text{H}_2}^{\text{s}} \quad [27]$$

where  $C_{\text{H}_2}^{\text{s}}$  denotes the concentration of hydrogen at the surface of the silicon wafer and  $K_{\text{r}}$  denotes the desorption rate constant, which is a function of temperature. The fraction of occupied sites at steady state is obtained from the following relation

$$\frac{\partial X}{\partial t} = R_{\text{ad}} - R_{\text{Si}} \quad [28]$$

Using Eq. 26, 27, and 28

$$X = \frac{K_{\text{ad}}C_{\text{SiHCl}_3}^{\text{s}}}{K_{\text{ad}}C_{\text{SiHCl}_3}^{\text{s}} + K_{\text{r}}C_{\text{H}_2}^{\text{s}}} \quad [29]$$

and from Eq. 27 and Eq. 29 the silicon deposition rate is obtained

$$R_{\text{Si}} = \frac{K_{\text{ad}}C_{\text{SiHCl}_3}^{\text{s}}}{1 + \frac{K_{\text{ad}}C_{\text{SiHCl}_3}^{\text{s}}}{K_{\text{r}}C_{\text{H}_2}^{\text{s}}}} \quad [30]$$

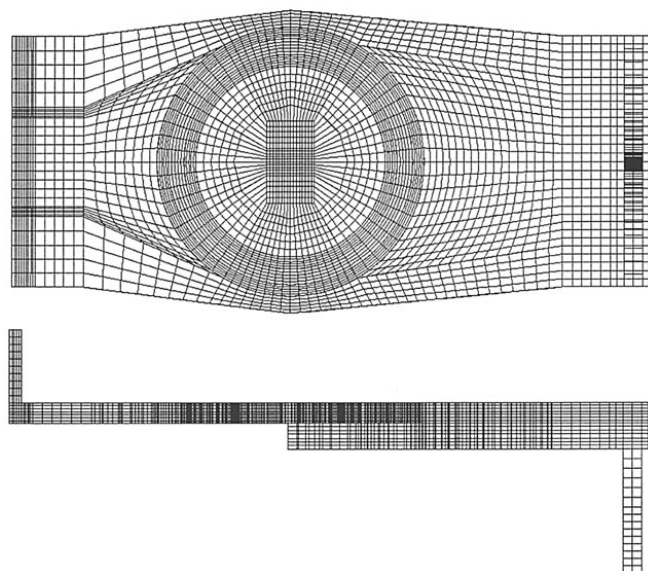


**Figure 11.** Domain discretization of the ASM Epsilon One reactor geometry. Total number of finite volume cells = 43,414. Top: projection of the mesh along the  $X$ - $Y$  midplane; bottom: projection of the mesh along the  $X$ - $Z$  midplane.

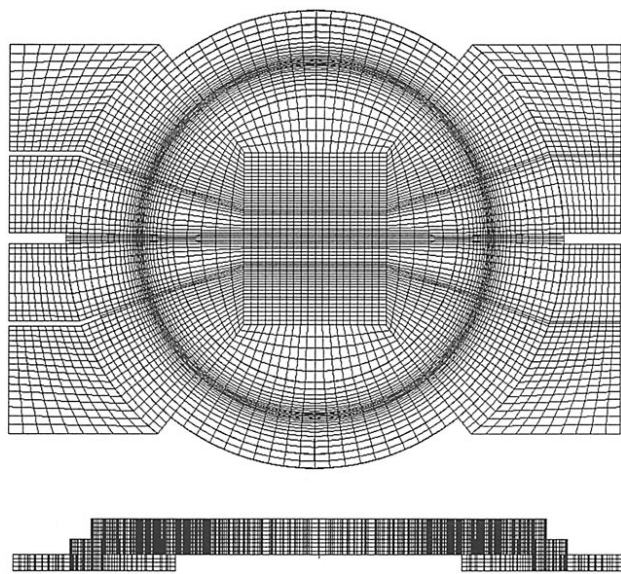


**Figure 12.** Domain discretization of the Applied Materials' Centura reactor geometry. Total number of finite volume cells = 46,320. Top: projection of the mesh along the X-Y midplane; bottom: projection of the mesh along the X-Z midplane.

In order to couple this phenomenological kinetic model of silicon deposition rate to the transport model one needs to determine  $K_{ad}$

**Table II.** Rate constants at different temperatures.

Temperature (K)	$K_f$ [ $m^4/(kmol\ s)$ ]	$K_{ad}$ (m/s)	$K_r$ (m/s)
1373	5.6	1.00	$3.83 \times 10^{-3}$
1398	7.0	1.00	$4.23 \times 10^{-3}$
1423	8.6	1.00	$4.63 \times 10^{-3}$

and  $K_r$ . This can be accomplished by experimentally measuring the silicon deposition rates on the leading edge of the hot wafer. The reason for selecting the leading edge of the hot wafer is that the mass-transfer resistance is almost negligible at this position due to the negligible thickness of the mass-transfer boundary layer. So one can assume that the concentration of  $SiHCl_3$  at the leading edge is close to the initial concentration of  $SiHCl_3$ . Therefore, by measuring the silicon deposition rate at the leading edge of the hot wafer at different temperatures one can determine the values of  $K_{ad}$  and  $K_r$  as functions of temperature. However, it is very difficult to experimentally measure the deposition rate at the leading edge of the hot wafer because in the commercial reactors used to perform experiments, the wafer sits on a hot graphite susceptor that is surrounded by a SiC ring. Due to this limitation we have decided to couple the proposed kinetics shown by Eq. 30 with a full three-dimensional simulation of mass, momentum, and energy transport in the reactor to determine  $K_{ad}$  and  $K_r$ . Specifically, simulations have been performed for various sets of  $K_r$  and  $K_{ad}$  at a fixed temperature. Figures 11 and 12 show the domain discretizations used to perform simulations of the ASM

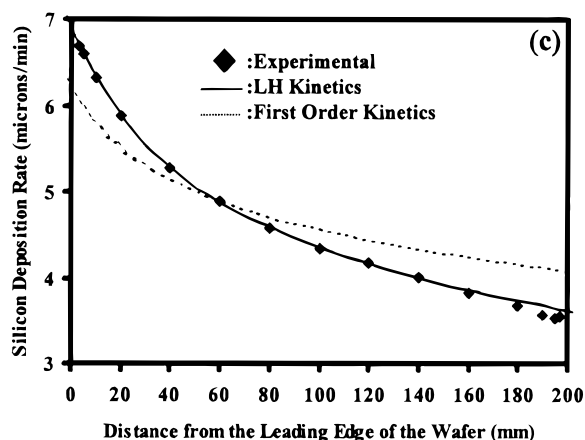
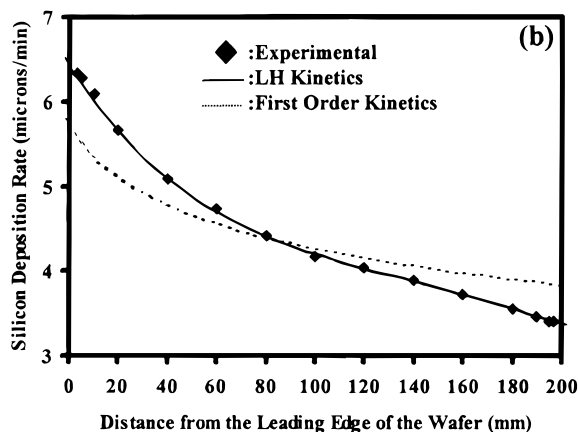
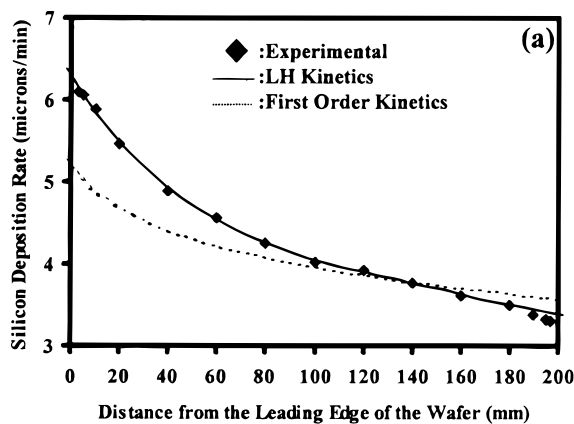


**Figure 13.** Theoretically predicted and experimentally measured silicon deposition rates in the flow direction along the centerline of the wafer as a function of wafer temperature for a fixed inlet volumetric flow rate of  $1.7 \times 10^{-3} \text{ m}^3/\text{s}$  and a fixed inlet gas composition of  $w_{SiHCl_3, in} = 0.71$ . Deposition rate is defined as the ratio of the deposited film thickness to the deposition time. Measurements from the two reactors are indistinguishable. (a)  $T = 1398 \text{ K}$ ; (b)  $T = 1423 \text{ K}$ ; (c)  $T = 1448 \text{ K}$ .

Epsilon One and the Applied Materials Centura reactors, respectively. To investigate the effect of various operating conditions on the silicon deposition rate a number of simulations have been performed with these meshes. To ensure that the solutions generated with the meshes shown in Fig. 11 and 12 are accurate, selected computations using a much more refined mesh consisting of approximately 200,000 cells were performed. Overall, we did not find a significant difference between the results from the two meshes, *i.e.*, the maximum difference between the computed results is less than 2%. Hence, the results shown below are based on the meshes shown in Fig. 11 and 12.

The computed and measured silicon deposition rates along the centerline of the wafer as a function of volumetric flow rate and gas composition have been used to determine  $K_f$  and  $K_{ad}$  at a fixed temperature. Specifically, a regression analysis was used to minimize the error between the simulated results and the experimental measurements as a function of  $K_{ad}$  and  $K_f$

$$\text{Error} = \sum_{x=1}^{x=N} (G_{x,\text{model}} - G_{x,\text{Experimental}})^2 \quad [31]$$

In Eq. 31,  $G_x$  is the silicon deposition rate at any position  $x$  along the centerline of the wafer and  $N$  is the total number of points on the wafer surface at which the deposited layer thickness is measured. The same procedure was repeated at different wafer temperatures. It

should be noted that  $K_f$  in the simple kinetic model (see Eq. 23) is also determined by a similar regression analysis. Table II shows the adsorption and desorption rate constants and  $K_f$  at the three different wafer temperatures considered. From the values of  $K_{ad}$  and  $K_f$  shown in Table II it is evident that the silicon deposition rate is more sensitive to the desorption rate constant compared to the value of the adsorption rate constant. This observation is fully consistent with the observations made by Ho *et al.*<sup>22</sup>

Figure 13, 14, and 15 show the comparisons between model predictions and experimental results. The experimental results shown in Fig. 13, 14, and 15 are typical silicon deposition rates obtained under normal operating conditions from the ASM and the Centura reactors. Figure 13 shows the model prediction of silicon deposition rate as a function of wafer temperature along the centerline of the wafer surface for a nonrotating wafer for a fixed inlet volumetric flow ( $1.7 \times 10^{-3} \text{ m}^3/\text{s}$ ) and fixed inlet composition ( $\text{SiHCl}_3$  mass fraction = 0.71). It should be noted that the units of silicon deposition rate in the plot are microns/minute and the units of  $R_{\text{Si}}$  are converted to microns/minute as  $G(\mu\text{m}/\text{min}) = R_{\text{Si}} \cdot 6.0 \cdot 10^7 \text{ Mw}_{\text{Si}}/\rho_{\text{Si}}$ . Figure 13 shows that the silicon deposition rate increases with an increase in the temperature of the wafer although the rate of increase is not very high in the temperature range considered in this study. Figure 13 also demonstrates that the Langmuir-Hinshelwood model is capable of predicting the experimentally observed decrease in silicon deposition rate from the leading edge to the trailing edge of the wafer at different temperatures. However, the linear kinetic model is inca-

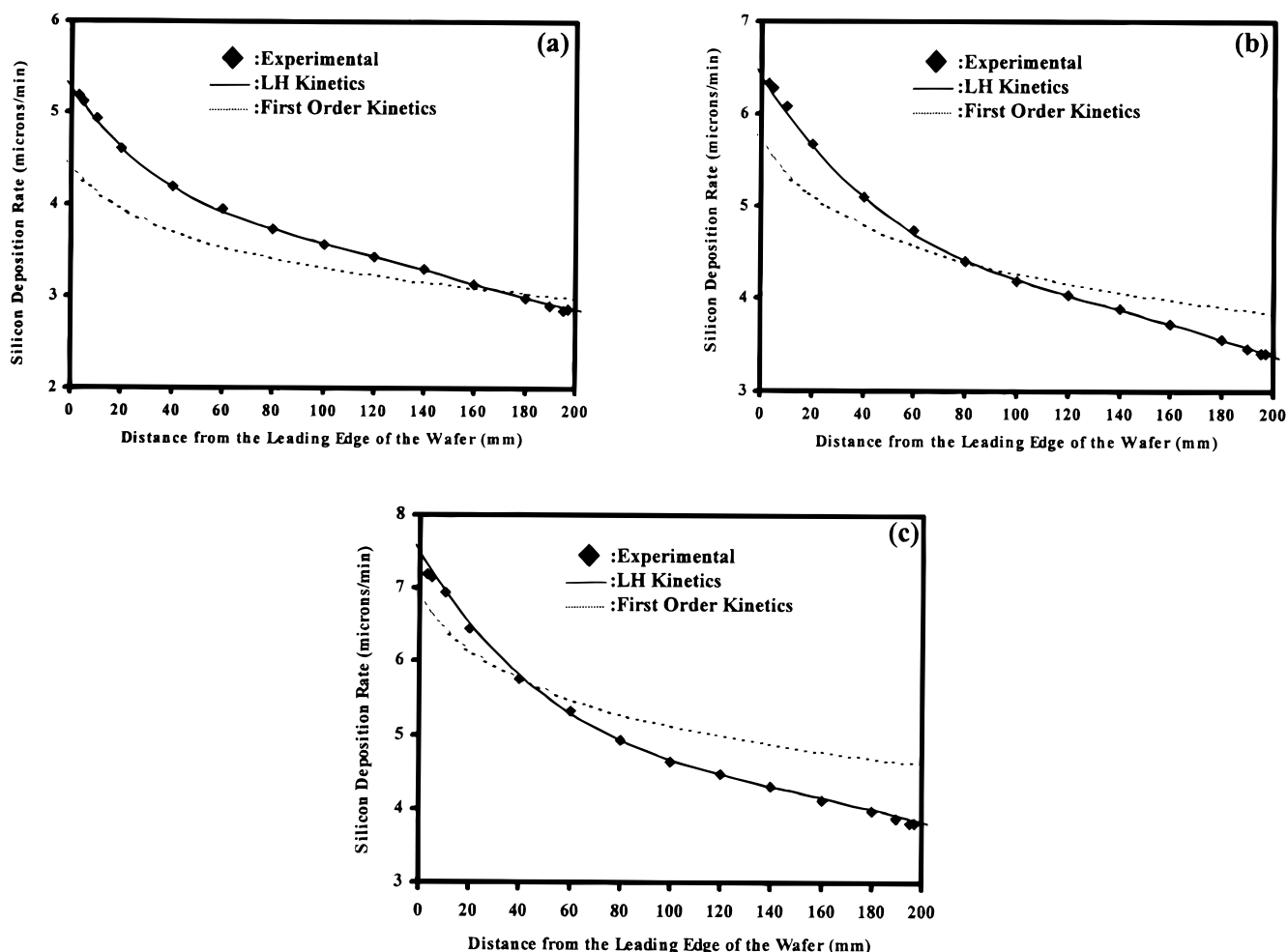


**Figure 14.** Theoretically predicted and experimentally measured silicon deposition rates in the flow direction along the centerline of the wafer as a function of inlet gas composition for a fixed inlet volumetric flow rate of  $1.7 \times 10^{-3} \text{ m}^3/\text{s}$  and a fixed wafer temperature of 1398 K. Deposition rate is defined as the ratio of the deposited film thickness to the deposition time. Measurements from the two reactors are indistinguishable. (a)  $w_{\text{SiHCl}_3, \text{in}} = 0.65$ ; (b)  $w_{\text{SiHCl}_3, \text{in}} = 0.71$ ; (c)  $w_{\text{SiHCl}_3, \text{in}} = 0.76$ .

pable of predicting this trend. This is due to the fact that the desorption mechanism is not accounted for in this model. Figure 14 depicts the model predictions of the silicon deposition rate as a function of the inlet  $\text{SiHCl}_3$  composition along the centerline of the wafer surface for a nonrotating wafer under conditions of a fixed inlet volumetric flow rate ( $1.7 \times 10^{-3} \text{ m}^3/\text{s}$ ) as well as a fixed wafer temperature of 1398 K. This figure clearly shows that, as expected, the silicon deposition rate increases with an increase in the inlet  $\text{SiHCl}_3$  concentration. Moreover, the proposed Langmuir-Hinshelwood kinetic model leads to excellent predictions of experimental results at the three different  $\text{SiHCl}_3$  concentrations while the simple linear kinetic model predictions are not very good. Figure 15 depicts the model prediction of silicon deposition rate as a function of inlet volumetric flow along the centerline of the wafer surface for a nonrotating wafer for a fixed inlet composition ( $\text{SiHCl}_3$  mass fraction = 0.71) and a fixed wafer temperature of 1398 K. As shown by this figure, an increase in volumetric flow rate leads to an increase in silicon deposition rate which essentially means that the rate of transport of chemical species plays an important role in determining the silicon deposition rate. Once again the Langmuir-Hinshelwood type of kinetic model predicts the experimental results well for the three volumetric flow rates considered. Overall, the above comparisons clearly demonstrate that a detailed transport model coupled with the Langmuir-Hinshelwood type kinetics is capable of predicting silicon deposition rates over a wide range of processing conditions and

hence can be used to effectively design and optimize CVD reactors with the  $\text{SiHCl}_3\text{-H}_2$  reactant system.

Although it is not possible to separate exactly the influence of mass transfer and kinetics on the silicon deposition rate from the above analysis, the simulation results clearly suggest that the silicon deposition rate in the region around the leading edge of the wafer is more sensitive to the reaction kinetics and the deposition rate at the trailing edge is more sensitive to the transport properties. This can be explained by the fact that near the leading edge the mass-transfer boundary layer is thin, hence the overall deposition rate is governed by the reaction rate. However, at the trailing edge the thickness of the mass-transfer boundary layer is significant, hence, the ability to rapidly get the reactants to the wafer surface becomes the controlling factor.

#### Effect of Wafer Rotation Rate on the Thickness Uniformity

Our experimental studies indicate that by rotating the wafer and adjusting the flow rate ratios across the three reactor inlets the thickness uniformity of the deposited silicon can be optimized. We have also observed that the simulated deposition rates and profiles for rotating and static wafers are very similar when the wafer is rotated with a speed in the range of 5-50 rpm (see Fig. 16). This is due to the fact that in this range of rotation speeds (*i.e.*, typical range used in industrial reactors) wafer rotation affects the flow field only in the close proximity of the wafer surface, hence the mass-transfer boundary layer thickness is almost unaffected. As a result, the bulk  $\text{SiHCl}_3$

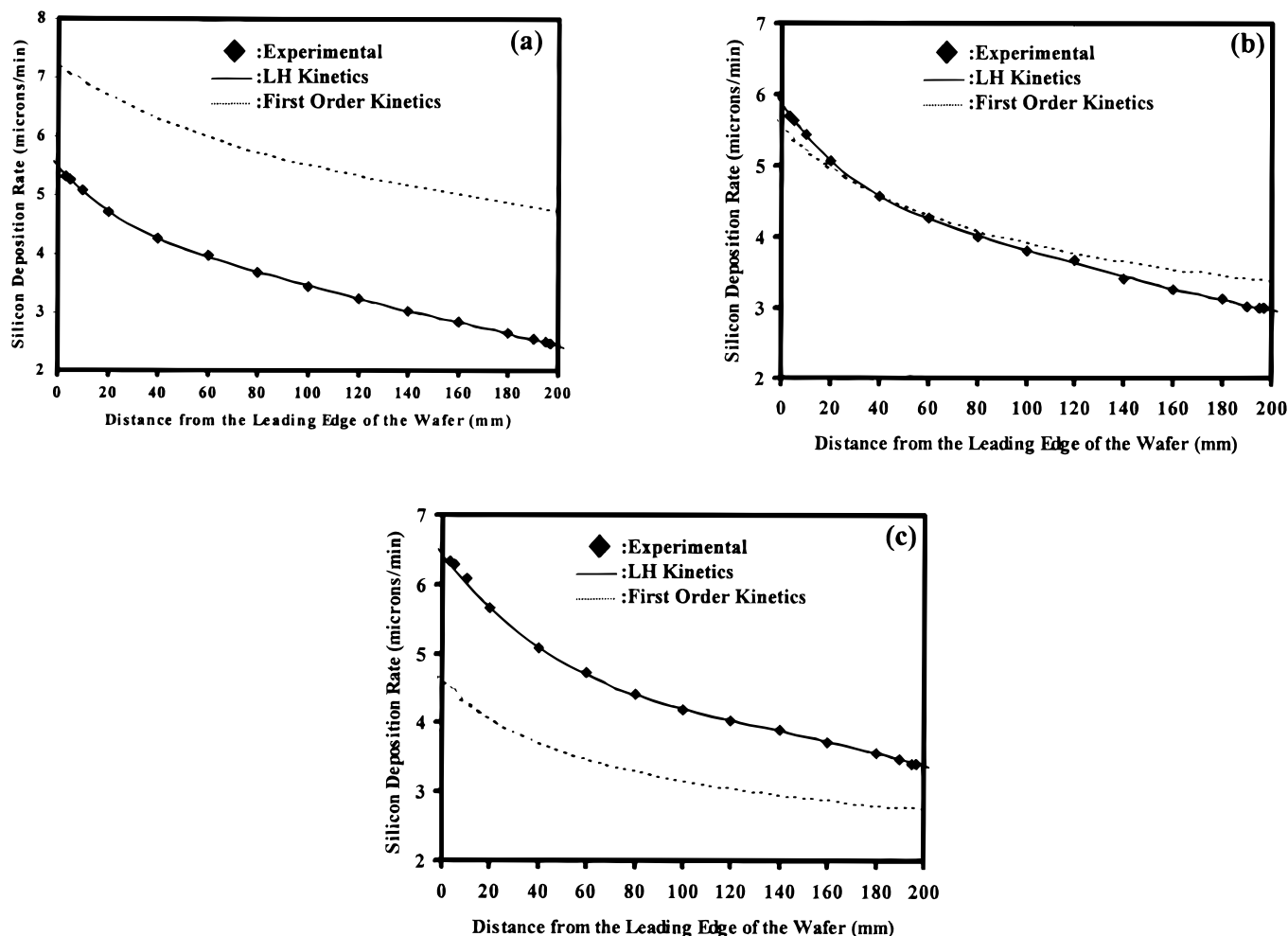


**Figure 15.** Theoretically predicted and experimentally measured silicon deposition rates in the flow direction along the centerline of the wafer as a function of inlet volumetric flow rate for a fixed inlet gas composition of  $w_{\text{SiHCl}_3} = 0.71$  and a fixed wafer temperature 1398 K. Deposition rate is defined as the ratio of the deposited film thickness to the deposition time. Measurements from the two reactors are indistinguishable. (a)  $1.1 \times 10^{-3} \text{ m}^3/\text{s}$ ; (b)  $1.7 \times 10^{-3} \text{ m}^3/\text{s}$ ; (c)  $2.4 \times 10^{-3} \text{ m}^3/\text{s}$ .

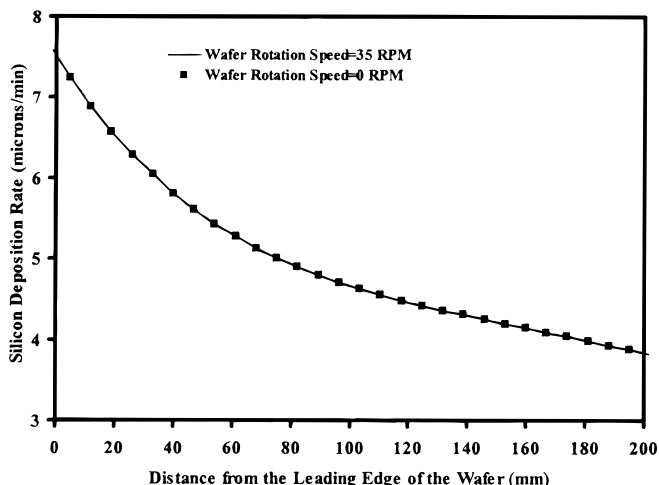


**Figure 16.** Comparison of silicon deposition rates in the flow direction along the centerline of the wafer with and without wafer rotation in the ASM reactor. Volumetric flow rate =  $1.7 \times 10^{-3} \text{ m}^3/\text{s}$ ;  $T = 1398 \text{ K}$ ;  $w_{\text{SiHCl}_3, \text{ in}} = 0.76$ .

concentration profile (*i.e.*,  $\text{SiHCl}_3$  concentration profile at a height midway from the wafer surface to the top of the reactor) remains the same irrespective of the wafer rotation speed (see Fig. 17).

Clearly, in the absence of wafer rotation, the deposition rate is nonuniform both in the direction of the flow (see Fig. 16) as well as in the transverse direction to the flow (see Fig. 18a). Hence, wafer rotation is required if good thickness uniformity is to be achieved since rotation translates any location on the wafer through both high (leading edge) and low (trailing edge) deposition regimes leading to azimuthal averaging. Hence, to compare the computed deposition rates with the experimental ones, the continuous change in the position of the wafer due to wafer rotation must be taken into consideration, *i.e.*, the film thickness at a given position on the wafer should be calculated by integrating the deposition rate over all the positions that are at the same distance from the wafer center. After integrating the local deposition rates along different radii, we have found that the numerical results using Langmuir-Hinshellwood kinetics compared very well with the experimental measurements (see Fig. 18b). Figure 18b also shows that for rotation speeds less than 50 rpm the deposition rate as function of radial position from the center is identical

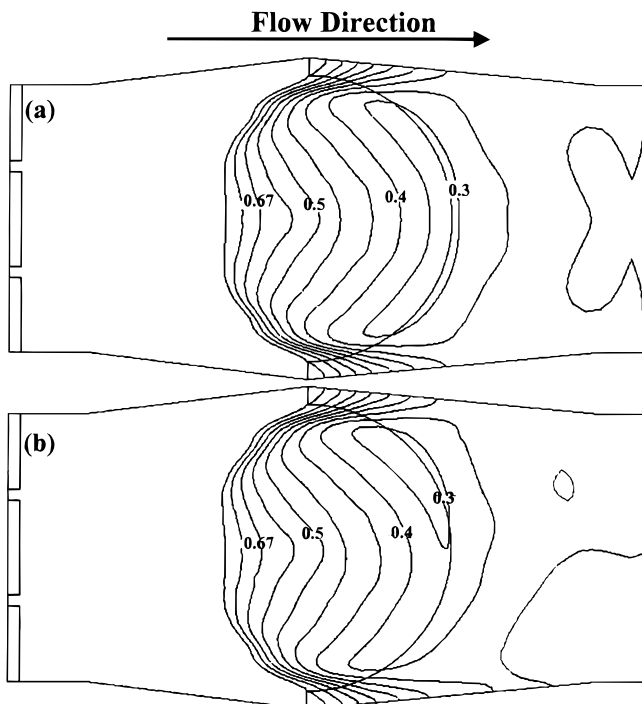


**Figure 17.**  $\text{SiHCl}_3$  mass-fraction profile along the X-Y midplane in the ASM reactor. Volumetric flow rate =  $1.7 \times 10^{-3} \text{ m}^3/\text{s}$ ;  $T = 1398 \text{ K}$ ;  $w_{\text{SiHCl}_3, \text{ in}} = 0.67$ . (a) Stationary wafer; (b) wafer rotated at 35 rpm.

for a rotating wafer and a stationary wafer when the deposition rate has been averaged in the azimuthal direction (thickness nonuniformity is defined as the percent difference between the thickness of the deposited layer at any location on the wafer with respect to the thickness of the deposited layer at the center of the wafer), confirming the fact that wafer rotation mainly leads to azimuthal averaging of the thickness of the deposited layer.

As wafer rotation mainly leads to azimuthal averaging of the thickness of the deposited layer, other strategies should be explored to control the silicon thickness uniformity in the radial direction. As mentioned above, this can be accomplished by adjusting the inlet flow rate ratios across the wafer. In fact it can be shown that adjust-

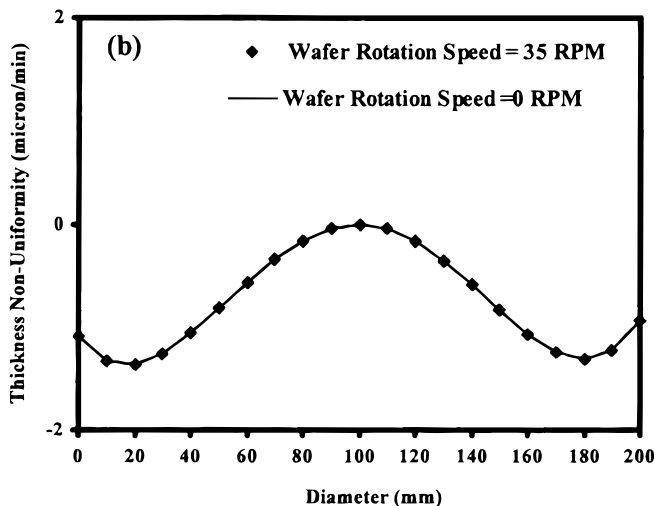
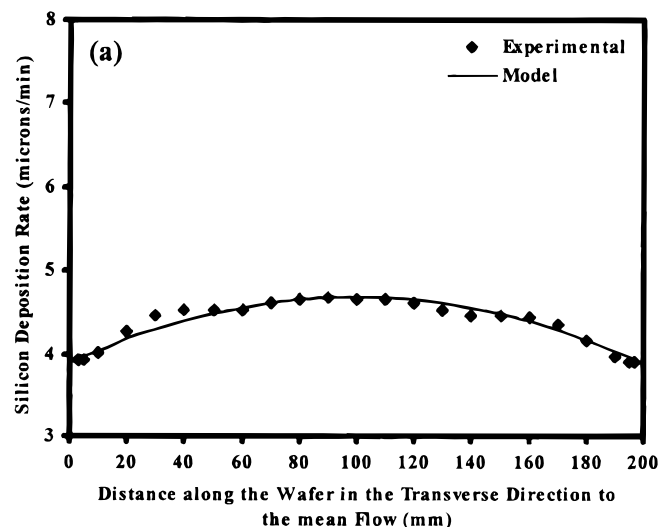


**Figure 18.** Silicon deposition rates as a function of wafer rotation speed. Volumetric flow rate =  $1.7 \times 10^{-3} \text{ m}^3/\text{s}$ ,  $T = 1398 \text{ K}$ ;  $w_{\text{SiHCl}_3, \text{ in}} = 0.76$ . Flow rate ratio across the inlets = 1.5:1. (a) Comparison of computed and experimentally measured silicon deposition rates in the transverse direction to the mean flow along the centerline on a stationary wafer. (b) Comparison of computed thickness nonuniformity in the radial direction as a function of wafer rotation rate. The center of the disk corresponds to position 100.

ing the inlet flow ratios has a major effect on the shape of the deposition rate profile in the radial direction. Figure 19 compares the numerical and experimental silicon thickness nonuniformity profiles obtained when the wafer is rotated with different inlet flow rate ratios. Figure 19 shows that for a wafer rotation speed of 35 rpm, when the gas velocity through all the three inlets is maintained the same a thickness nonuniformity of 7% is obtained with the thickness at the edge of the wafer being greater than the thickness at the center giving rise to a U-shaped thickness profile. This is very undesirable because the thickness nonuniformity should generally meet a specification of less than 2% for an industrial accepted quality epitaxial silicon wafer. Figure 19 shows that when the gas velocity through inlet 2 is increased to twice the gas velocity through inlet 1 and inlet 3 an inverted U-shaped thickness profile with a thickness nonuniformity close to 7% is obtained. Figure 19 also shows that for a flow rate ratio of 1.5:1 between the central to the side inlets an acceptable thickness nonuniformity (*i.e.*, a less than 2% variation across the wafer) is obtained. The above simple analysis shows that by adjusting the gas flow rates through the three gas inlets (*i.e.*, varying the rate of mass transport to different sections of the wafer) one can optimize the epitaxial thickness uniformity on the wafer.

### Summary

A simulation model for horizontal single-wafer epitaxial silicon atmospheric CVD reactors has been developed. In the development of the model the dependence of the gas properties on the gas composition and temperature as well as mass transport due to thermal diffusion have been considered. As SiHCl<sub>3</sub> is a widely used precursor for growing epitaxial films in industrial applications the simulation model has been used to study the epitaxial silicon deposition from a SiHCl<sub>3</sub>-H<sub>2</sub> precursor. To examine the predictive capability of the simulation model, a selected number of silicon epitaxial deposition experiments were performed in two commercial CVD reactors. A detailed comparison of simulation and experimental results has indicated that a detailed transport model that includes mass transport due to thermal diffusion in conjunction with a Langmuir-Hinshelwood type kinetic model for SiHCl<sub>3</sub> decomposition accurately describes the epitaxial silicon deposition process in a broad range of operating conditions. In turn, this lumped reaction kinetic model has been successfully used for optimization of commercially available horizontal CVD reactors.

### Acknowledgments

This work has been supported by a grant from MEMC Electronic Materials, Inc. We are grateful to Tom Torack for performing the deposition experiments as well as Dr. Robert W. Standley and Dr. Sriram Ramanathan for helpful comments.

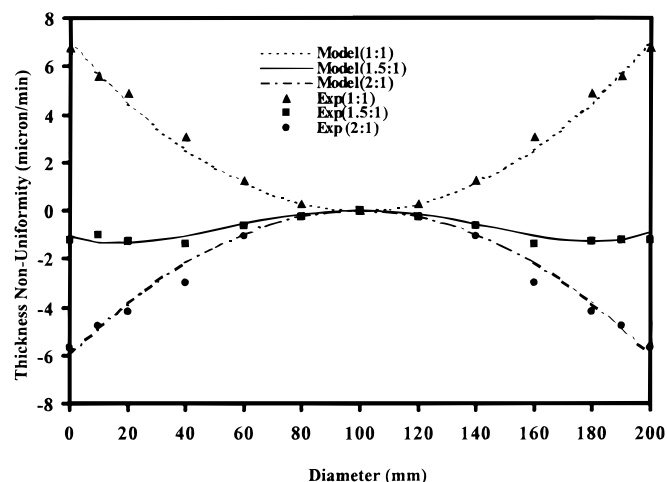


**Figure 19.** Theoretically predicted and experimentally measured silicon thickness profiles as a function of inlet gas flow rate ratios in the ASM reactor. Volumetric flow rate =  $1.7 \times 10^{-3} \text{ m}^3/\text{s}$ ;  $T = 1398 \text{ K}$ ;  $w_{\text{SiHCl}_3, \text{in}} = 0.67$ .

Washington University assisted in meeting the publication costs of this article.

### Appendix A

Specific heat as a function of temperature  
 [J/(kg K)]

Gases	Specific heat as a function of temperature [J/(kg K)]
Hydrogen	$1.408 \cdot 10^4 + 6.33 \cdot 10^{-1} T$
Trichlorosilane	$5.96 \cdot 10^2 + 6.76 \cdot 10^{-2} T$
HCl	$8.09 \cdot 10^2 - 5.5 \cdot 10^{-2} T + 7.20 \cdot 10^{-5} T^2 - 1.34 \cdot 10^{-8} T^3$

The specific heat of the gas mixture is calculated using the following relationship

$$C_{p\text{SiHCl}_3\text{-H}_2} = w_{\text{SiHCl}_3} C_{p\text{SiHCl}_3} + w_{\text{H}_2} C_{p\text{H}_2} \quad [\text{A-1}]$$

Viscosity as a function of temperature  
 (Pa s)

Gases	Viscosity as a function of temperature (Pa s)
Hydrogen	$3.0 \cdot 10^{-6} + 2.0 \cdot 10^{-8} (T/298) - 3.0 \cdot 10^{-12} (T/298)^2$
Trichlorosilane	$2.0 \cdot 10^{-7} + 4.0 \cdot 10^{-8} (T/298) - 5 \cdot 10^{-12} (T/298)^2$
HCl	$4.0 \cdot 10^{-7} + 5.0 \cdot 10^{-8} (T/298) - 8.0 \cdot 10^{-12} (T/298)^2$

The viscosity of the gas mixture is calculated using the following relationship:

$$\mu_{\text{mix}} = \sum_{i=1}^n \frac{x_i \mu_i}{\sum_{j=1}^n x_j \Phi_{ij}} \quad [\text{A-2}]$$

where

$$\Phi_{ij} = \frac{1}{\sqrt{8}} \left( 1 + \frac{M_i}{M_j} \right)^{-\frac{1}{2}} \left( 1 + \left( \frac{\mu_i}{\mu_j} \right)^{\frac{1}{2}} \left( \frac{M_j}{M_i} \right)^{\frac{1}{4}} \right)^2 \quad [\text{A-3}]$$

Thermal conductivity as a function of temperature  
 (W/m K)

Gases	Thermal conductivity as a function of temperature (W/m K)
Hydrogen	$4.7 \cdot 10^{-2} + 5.0 \cdot 10^{-4} (T) - 6.0 \cdot 10^{-8} (T)^2$
Trichlorosilane	$6.2 \cdot 10^{-3} + 5.0 \cdot 10^{-5} (T) - 7.0 \cdot 10^{-9} (T)^2$
HCl	$1.0 \cdot 10^{-4} + 5.0 \cdot 10^{-5} (T) - 3.0 \cdot 10^{-9} (T)^2$

The thermal conductivity of the gas mixture is calculated using the following relationship

$$\lambda = \xi \sum_{i=1}^n \lambda_i x_i + (1 - \xi) \sum_{i=1}^n \left( \frac{x_i}{\lambda_i} \right)^{-1} \quad [\text{A-4}]$$

where

$$\xi = 0.312 + 0.325x_{\text{H}_2} - 0.311x_{\text{H}_2} + 0.469x_{\text{H}_2} \quad [\text{A-5}]$$

The expressions A-2 to A-4 are obtained from Bretsznajder.<sup>29</sup>

### Appendix B

Binary diffusion coefficients as a function of temperature ( $\text{m}^2/\text{s}$ )

Gas pairs	Binary diffusion coefficients as a function of temperature ( $\text{m}^2/\text{s}$ )
Hydrogen-hydrogen	$4.0 \cdot 10^{-5} (T/298) + 10^{-4} (T/298)^2 - 8.0 \cdot 10^{-6} (T/298)^3 + 5.0 \cdot 10^{-4} (T/298)^4$
Trichlorosilane-hydrogen	$7.0 \cdot 10^{-6} (T/298) + 3.0 \cdot 10^{-5} (T/298)^2 - 3.0 \cdot 10^{-6} (T/298)^3 + 2.0 \cdot 10^{-4} (T/298)^4$
HCl-hydrogen	$2.0 \cdot 10^{-5} (T/298) + 5.0 \cdot 10^{-5} (T/298)^2 - 3.0 \cdot 10^{-6} (T/298)^3 + 7.0 \cdot 10^{-8} (T/298)^4$

The thermal diffusion coefficients of the gas species are calculated using the following relationships

$$D_{\text{SiHCl}_3}^T = \frac{P}{MRT} M_{\text{SiHCl}_3} M_{\text{H}_2} D_{\text{SiHCl}_3\text{-H}_2} k_{\text{SiHCl}_3\text{-H}_2} \quad [\text{B-1}]$$

$$D_{\text{HCl}}^T = \frac{P}{MRT} M_{\text{HCl}} M_{\text{H}_2} D_{\text{HCl-H}_2} k_{\text{HCl-H}_2} \quad [\text{B-2}]$$

where the thermal diffusion ratios ( $k_{\text{HCl-H}_2}$  and  $k_{\text{SiHCl}_3\text{-H}_2}$ ) are obtained as a function of the gas species concentrations and temperature from Hirshfelder *et al.*<sup>30</sup>

### List of Symbols

$C_A$	molar concentration of chemical species A (kmol m <sup>-3</sup> )
$C_{pA}$	specific heat of chemical species A (J kg <sup>-1</sup> K <sup>-1</sup> )
$Da$	Damkohler number
$D_{AB}$	binary diffusion coefficient of chemical species A in diluent B (m <sup>2</sup> s <sup>-1</sup> )
$D_A^T$	thermal diffusion coefficient of chemical species A in diluent B (kg m <sup>-1</sup> s <sup>-1</sup> )
$e_z$	Unit normal vector along $z$ direction
$g$	acceleration due to gravity (m s <sup>-2</sup> )
$Ga$	Gay-Lussac number
$Gr$	Grashof number
$G_x$	silicon deposition rate at any position $x$ on the wafer surface (μm min <sup>-1</sup> )
$h$	heat transfer coefficient (W m <sup>-2</sup> K <sup>-1</sup> )
$j_A^C$	diffusion flux of chemical species A driven by concentration gradient (kg m <sup>-2</sup> s <sup>-1</sup> )
$j_A^T$	diffusion flux of chemical species A driven by temperature gradient (kg m <sup>-2</sup> s <sup>-1</sup> )
$K_{ad}$	adsorption rate constant (m s <sup>-1</sup> )
$K_f$	reaction rate constant (m <sup>4</sup> kmol <sup>-1</sup> s <sup>-1</sup> )
$K_r$	desorption rate constant (m s <sup>-1</sup> )
$L$	characteristic reactor dimension (m)
$Mw_A$	molecular weight of a gas species A (kg kmol <sup>-1</sup> )
$\mathbf{n}$	unit normal vector
$P$	pressure (Pa)
$Pr$	Prandtl number
$R$	universal gas constant (J kmol <sup>-1</sup> K <sup>-1</sup> )
$R_A$	surface chemical reaction rate of chemical species A (kg m <sup>-2</sup> s <sup>-1</sup> )
$R_{ad}$	rate of adsorption (kmol m <sup>-2</sup> s <sup>-1</sup> )
$Re$	Reynolds number
$R_{si}$	silicon deposition rate (kmol m <sup>-2</sup> s <sup>-1</sup> )
$Sc$	Schmidt number
$T$	temperature (K)
$Td$	thermal diffusion number
$T_{inf}$	ambient gas temperature (K)
$T_{wafer}$	wafer surface temperature (K)
$T_{wall}$	wall temperature (K)
$U$	velocity of gas (m s <sup>-1</sup> )
$V$	characteristic velocity of gas (m s <sup>-1</sup> )
$w_A$	mass fraction of chemical species A
$w_{A,in}$	mass fraction of chemical species A at the reactor inlets
$X$	fraction of reactive sites on wafer surface occupied by SiHCl <sub>3</sub>

$\rho$	density of gas (kg m <sup>-3</sup> )
$\mu$	viscosity of gas (kg m <sup>-1</sup> s <sup>-1</sup> )
$\lambda$	thermal conductivity of gas (W K <sup>-1</sup> )
$\wedge$	dimensionless parameter

### References

- C. R. Kleijn, Ph.D. Thesis, Delft University of Technology, Delft, The Netherlands (1991).
- K. F. Jensen, H. Simka, T. G. Mihopoulos, P. Futerko, and M. Hierlemann, in *Advances in Rapid Thermal and Integrated Processing*, F. Roozboom, Editor, Series E: Applied Sciences, Vol. 318, p. 305, Kluwer Academic Publishers, Amsterdam (1995).
- H. Schlichting, *Boundary-Layer Theory*, 7th ed., McGraw-Hill, New York (1968).
- G. Evans and R. Grief, *Num. Heat Transfer*, **14**, 373 (1988).
- V. J. Ven, G. J. M. Rutten, M. J. Raaymakers, and L. J. Giling, *J. Cryst. Growth*, **76**, 352 (1986).
- C. Weber, C. Opedorp, and M. Keijsers, *J. Appl. Phys.*, **67**, 2109 (1990).
- D. I. Fotiadis, S. Kieda, and K. F. Jensen, *J. Cryst. Growth*, **102**, 441 (1990).
- H. K. Moffat and K. F. Jensen, *J. Cryst. Growth*, **77**, 108 (1986).
- H. K. Moffat and K. F. Jensen, *J. Electrochem. Soc.*, **135**, 459 (1988).
- C. Kleijn and C. J. Hoogendoorn, *Chem. Eng. Sci.*, **46**, 321 (1991).
- M. E. Coltrin, R. J. Kee, and J. A. Miller, *J. Electrochem. Soc.*, **131**, 425 (1984).
- M. E. Coltrin, R. J. Kee, and G. H. Evans, *J. Electrochem. Soc.*, **136**, 819 (1989).
- J. Ouazzani, K. Chiu, and F. Rosenberger, *J. Cryst. Growth*, **91**, 497 (1988).
- H. Habuka, M. Katayama, M. Shimada, and K. Okuyama, *Jpn. J. Appl. Phys.*, **33**, 1977 (1994).
- H. Habuka, T. Nagoya, M. Katayama, M. Shimada, and K. Okuyama, *J. Electrochem. Soc.*, **142**, 4272 (1995).
- H. Habuka, T. Nagoya, M. Mayasumi, M. Katayama, M. Shimada, and K. Okuyama, *J. Cryst. Growth*, **169**, 61 (1996).
- CFX 4.1c Solver*, AEA Technology, CFX International, Oxfordshire, U.K. (1997).
- S. V. Patankar, *Numerical Heat Transfer and Fluid Flow*, Hemisphere Publ. Corp., Washington, DC (1983).
- H. L. Stone, *SIAM J. Num. Anal.*, **7**, 104 (1968).
- R. D. Lonsdale, *Int. J. Num. Meth. Heat Fluid Flow*, **3**, 553 (1993).
- ECO Software User's Guide*, Nicolet Instrument Corporation, Madison, WI (1994).
- P. Ho, A. Balakrishna, M. J. Chacin, and A. Thilderkvist, in *Fundamental Gas-Phase and Surface Chemistry of Vapor-Phase Materials Synthesis*, M. D. Allendorf, M. R. Zachariah, L. Mountziaris, and A. H. McDaniel, Editor, Vol. 98-23, p. 117, The Electrochemical Society Proceeding Series, Pennington, NJ (1998).
- K. L. Walker, R. E. Jardine, M. A. Ring, and H. E. O'Neal, *Int. J. Chem. Kinet.*, **30**, 69 (1998).
- M. D. Su and H. B. Schlegel, *J. Phys. Chem.*, **97**, 9981 (1993).
- M. T. Swihart and R. W. Carr, *J. Phys. Chem.*, **A102**, 1542 (1998).
- P. Ho, M. E. Coltrin, J. S. Binkley, and C. F. Melius, *J. Phys. Chem.*, **89**, 4647 (1985).
- M. A. Mendicino and E. G. Seebauer, *J. Electrochem. Soc.*, **140**, 1786 (1993).
- P. Bratu, K. L. Kompa, and U. Hofer, *Chem. Phys. Lett.*, **251**, 1 (1996).
- S. Bretznajder, *Prediction of Transport and other Physical Properties of Fluids*, Pergamon Press, Oxford (1971).
- J. O. Hirschfelder, C. F. Curtiss, and R. B. Bird, *Molecular Theory of Gases and Liquids*, John Wiley & Sons, Inc., New York (1967).